Thermal Science and Engineering Progress 43 (2023) 101987

Contents lists available at ScienceDirect

Thermal Science and Engineering Progress

journal homepage: www.sciencedirect.com/journal/thermal-science-and-engineering-progress

Hydrothermal behavior of nanofluid flow in a microscale backward-facing step equipped with dimples and ribs; Lattice Boltzmann method approach

Saboura Yousefi [a], Mostafa Mahdavi [a,*], Seyed Soheil Mousavi Ajarostaghi [b,c], Mohsen Sharifpur [a,d,*]

[a] Department of Mechanical and Aeronautical Engineering, University of Pretoria, Pretoria 0002, South Africa
[b] Mechanical Engineering Department, Université de Sherbrooke (UdeS), Sherbrooke, QC J1K 2R1, Canada
[c] Department of Mechanical Engineering, Babol Noshirvani University of Technology, Babol, Iran
[d] Department of Medical Research, China Medical University Hospital, China Medical University, Taichung, Taiwan

ARTICLE INFO

Keywords:
Microchannel
Lattice Boltzmann Method
Backward-Facing Step
Nanofluid
Heat Transfer

ABSTRACT

Due to rapid development in the technology of electronic devices and improved performance of thermoelectric materials, thermal management is one of the significant issues to be dealt with. Hence, the conventional heat transfer methods are not responsive anymore, especially in micro-electric applications. In this work, the application of nanofluid, instead of pure fluids, in the microchannel heat sink with sudden explanation and insertion of ribs and dimples inside the backward-facing step microchannel is studied numerically. Lattice Boltzmann method is applied to study the heat transfer and laminar flow behaviour of 4% concentration of Al_2O_3-water nanofluids in Reynolds numbers ranging 40–100 through the backward-facing step microchannel. Microchannel size is 60 μm (H) × 60 μm (W) × 336 μm (L), and the height of the microchannel's step is 27 μm, and located 108 μm from the entrance. The bottom wall of the microchannel, downstream of the step is exposed to constant heat flux. Ribs and hemispherical dimples are located on this wall section as vortex generators. A few studies focus on curved boundaries in Lattice Boltzmann Method due to some complexities in curved boundaries, especially spherical ones. So, the main novelty of this work is inserting hemispherical dimples in backward-facing step microchannel and combining them with ribs as proposed turbulators. The results showed that increasing the number of ribs from 4 to 8 (100% growth) leads to a 63.64 and 64.65% augmentation in the average Nusselt number at Re = 40 and 100, respectively. Also, increasing the ribs heights from 0.5H to 2H (300% growth) caused average Nusselt number augmentation of about 54.54 and 40.91% at Re = 40 and 100, respectively. In some cases, with lower numbers or shorter ribs, the effects of adding ribs on the Nusselt number are either minor or undesirable.

Introduction

In recent years, due to the rapid development in the technology of electronic devices and improved performance of thermoelectric materials, thermal management is one of the significant issues to be dealt with. Due to higher heat dissipation in microprocessors, the conventional air-cooled cooling systems were insufficient. Hence high-performance cooling solutions such as liquid–vapour phase change, liquid cooling, heat pipes, nanoparticles-fluid suspension instead of conventional fluids, microchannel heat sink and sudden explanation or compression in systems were introduced [1–6]. Utilization of microchannel and microdevices in micro cooling systems, heat exchangers are growing rapidly due to the growing application of microfluidic technology and micro-electro-mechanical systems (MEMS). Microchannels enhance heat transfer efficiency due to a larger ratio of surface to volume. Another structural modification to achieve higher heat transfer performance is. The separation and reattachment of the flow resulting from sudden explanation or compression in flow passages lead to an improvement in heat transfer of the fluids. Hence, backward-facing steps or forward-facing steps are critical in industrial applications and engineering designs [7–14].

Although applying backward-facing steps is not desirable in some applications because of energy losses and pressure drops, which lead to

* Corresponding authors.
E-mail addresses: u11297362@up.ac.za (S. Yousefi), mostafa.mahdavi@up.ac.za (M. Mahdavi), seyed.soheil.mousavi.ajarostaghi@usherbrooke.ca (S. Soheil Mousavi Ajarostaghi), mohsen.sharifpur@up.a.za (M. Sharifpur).

https://doi.org/10.1016/j.tsep.2023.101987
Received 28 February 2023; Received in revised form 23 May 2023; Accepted 26 June 2023
Available online 29 June 2023

Nomenclature

k	Thermal conductivity ($W/m.k$)
c_p	Specific heat capacity ($J/kg.K$)
r_p	Nanoparticle's radius (m)
d_p	Nanoparticle's diameter (m)
t_l	Nanolayer thickness (m)
T	Temperature (K)
T_0	Absolut Temperature (K)
Nu	Nusselt number
Re	Reynolds number
D_h	Hydraulic diameter (m)
q	Heat flux (W/m^2)
e_i	Lattice velocity direction
f	Distribution function
f_{eq}	Equilibrium Distribution Function
g	Temperature distribution function
g_{eq}	Equilibrium temp. distribution function
u	velocity (m/s)
$\dot{m}$	Mass flow rate (kg/m^3)
c	Velocity vector
c_s	Speed of sound
w_i	Weight factor in ith direction
X	Dimensionless coordinate in X direction
Y	Dimensionless coordinate in Y direction
Z	Dimensionless coordinate in Z direction
h	Convective Heat transfer coefficient ($W/m^2.K$)

Greek symbols

ν	Kinematic viscosity (m^2/s)
φ	Volume concentration
α	Heat diffiusivity (m^2/s)
τ	Relaxation time
ρ	Density (kg/m^3)
μ	Dynamic Viscosity ($kg/m.s$)

Subscripts

p	Particle
pe	Equivalent particle
f	Base fluid
w	Wall
b	Bulk
eff	Effective
nf	Nanofluid
l	Nanolayer
i	Discrete lattice directions

Abbreviations

LBM	Lattice Boltzmann Method
MD	Molecular Dynamics
BFS	Backward-facing step
MBFS	Backward-facing step microchannel

extra pumping power, their benefits are significant enough not to be denied, especially in heating or cooling applications. In the backward-facing steps (BFSs), a sudden expansion occurs in flow transit and results in flow separation in the step edge. This phenomenon divides the flow into separation, recirculation, and reattachment regions. These separation, circulation and reconnection lead to higher mixing in mass and energy and, subsequently, higher heat transfer desired in heat exchangers, chemical processes, electronic devices, turbine blade cooling systems, chemical process equipment, combustion chambers and cooling of nuclear reactors. Many experimental and numerical studies address heat transfer and flow behaviour in the presence of sudden expansion or compression.

Applying BFSs in micro-sized channels has attracted considerable interest as it allows us to benefit from both in different applications. Many studies with the focus area of microchannels and BFSs applications were observed [9–18]. Inserting obstacles in the flow path leads to the creation of vortex and flow fluctuation for mixing of fluids with different temperature, and in some cases, direct the flow to move closer to the desired wall. Sometimes adding the obstacles increases the contact surface; hence higher thermal transport could be achieved. Depending on the reason for applying, these obstacles were named baffles, barriers, ribs, vortex generators, turbulator, etc. Hence studying the effects of choosing different shapes, sizes, locations, and numbers of these obstacles is essential. Several researchers have focused on utilizing baffles or a barrier in the flow passage. Johnson and Joubert [10] studied heat transfer enhancement caused by inserting different shapes of wings and winglets as vortex generators in tubes. Yeung and Kot [11] proposed a 2D boy-fitted curvilinear approach to study flow over other structures. Chen et al., [12] applied LBM to study the hydraulic and thermal behaviour of flow in the BFS channel. Also they inserted a cylindrical object downstream of step to study the effects of interruptions in the flow path. They concluded an increase in the average Nusselt number and the heat transfer. Selimefendigil and Oztop [13] studied Cu-Water nanofluid forced convection flow in a corrugated BFS channel with added circular, diamond and square-shaped obstacles and Reynolds number of 10–200. The numerical simulation revealed recirculation regions appearance depends on Reynolds number. Alkumait et al., [14] investigated a BFS by installing a baffle on the top wall. This numerical study was conducted based on the forced laminar flow of water in a channel with Reynolds number ranging 50–400. The results showed maximum average Nusselt number happened when the baffle was closest to the entrance after the step, the lowest Nusselt number belonged to the case with the channel without any baffle installed. Ahmed et al., [15] added different types of vortex generators on the top wall of a BFS microchannel in different shapes with varying angles of attack. The results show applying vortex generators enhance thermal performance. Hanji et al., [17] used the finite element method (FEM) to study the flow through the microchannel with sudden expansion or contraction. The size of the recirculation area increases by increasing the Reynolds number, which leads to an enhanced Nusselt number. Also they studied the effects of the number of obstacles and concluded increasing obstacle numbers leads to increased heat transfer [18]. Ekiciler and Çetinkaya [19] numerically investigated the impact of applying different shapes of ribs in a duct in a turbulent regime. They concluded the vortex caused by ribs leads to heat transfer enhancement due to disturbance of the thermal boundary layer.

Utilizing nanofluids with higher heat transfer performance substitutes conventional heat transfer fluids to overcome the heat transfer boundaries [20]. Choi [20] proposed using nanofluids, solid–liquid composite materials consisting of nanometer-sized solid particles, fibres, rods or tubes suspended in various base fluids. Numerous studies defined nanofluid properties to introduce nanofluids into industrial design and applications [22–32]. The volume fraction of the nanoparticles, temperature, nanoparticle size, nanolayer, the base fluid's thermal conductivity, the nanofluid's PH, and the nanoparticles' thermal conductivity were addressed as important parameters affecting nanofluid properties [22–23].

In systems with higher heat transfer requirements, replacing the conventional fluid with nanofluids is a significant optimisation step, especially in micro-sized applications. A considerable number of studies investigated the heat transfer and flow behaviour of nanofluids in microchannels, or the BFSs [17–23]. Kherbeet et al., [26] applied the

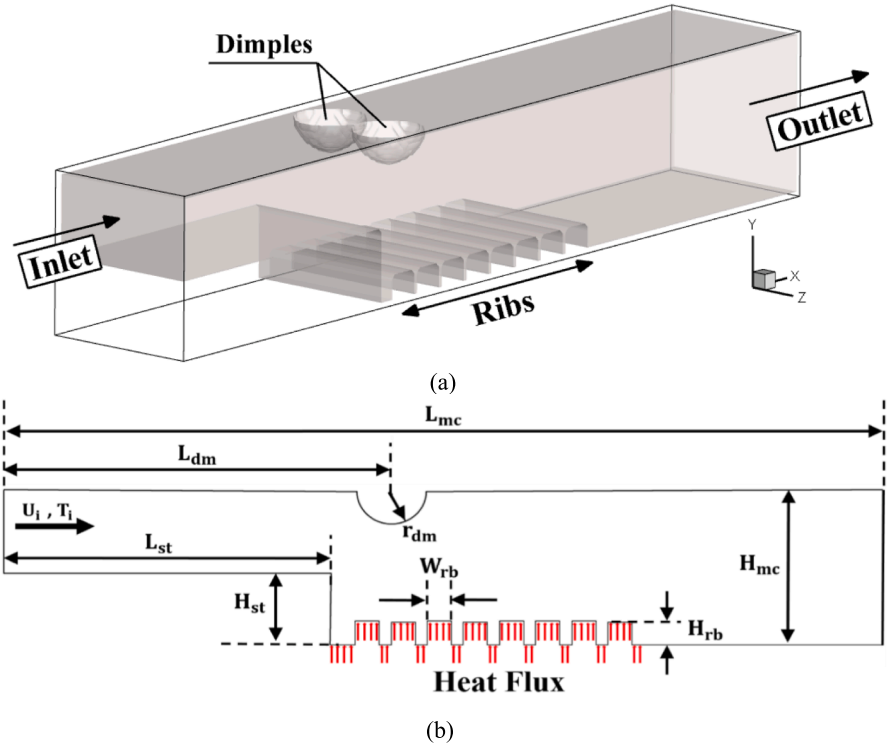

Fig. 1. (a) 3D View of the proposed microchannel, and (b) 2D schematic view of the backward-facing microchannel.

Table 1
The values of the microchannel's dimensions.

Description	Symbol	Size [mm]
Microchannel's Total Length	L_{mc}	33.6×10^{-2}
Microchannel's Downstream Height	H_{mc}	6.0×10^{-2}
Microchannel's Width	W_{mc}	6.0×10^{-2}
Step Height	H_{st}	2.7×10^{-2}
Microchannel's Upstream Length	L_{st}	10.8×10^{-2}
Hemispherical Dimples Radius	R_{dm}	1.3×10^{-2}
Hemispherical Dimples' Distance to Inlet	L_{dm}	13.0×10^{-2}
Length of Microchannel Wall with Heat Flux	L_{hf}	11.7×10^{-2}
Square Rib's Height	H_{rb}	0.9×10^{-2}
Square Rib's Width	W_{rb}	0.9×10^{-2}

three-dimensional finite volume method (FVM) to study EG-SiO_2 nanofluid through a backward-facing step microchannel in a laminar regime with a Reynolds number of 35. They observed a more eddy flow pattern close to the side walls, which increases with increasing step height. Also, they concluded higher step leads to Nusselt number and recirculation length enhancement and decreasing pressure drop and friction factor coefficient. Yang et al., [28] numerically and experimentally investigated applying nanofluids and BFSs to enhance heat transfer in microchannels and concluded both nanofluids and BFSs improve heat transfer. Ekiciler [29]studied nanofluids and hybrid nanofluids' heat transfer and flow behaviour numerically. The nanofluids flow in a duct with triangular ribs was analyzed using the RNG k-ε turbulence model. The results show the optimum nanofluid type, rib heights, position and size.

Lattice Boltzmann Method is applied for the computational study of this work. One of the advantages of this method is that it is easier to implement than other numerical methods like computational fluid dynamics (CFD), especially in complex geometries, multiphase, and multicomponent domains. Lattice Boltzmann Method operates between two macroscopic and microscopic scales, originating from the Lattice Gas Automata (LGA) method. This method monitors the behaviour of a group of particles instead of individual particles. Many researchers applied different approaches in LBM studies [33–46]. Shan and Chen [35] applied LBM to model fluids with immiscible components or single components with phase transition at a constant temperature. For this purpose, they considered non-local interaction between particles and introduced a term as inter-particle potentials. Xuan and Yao [37] used LBM to simulate the morphology of nanoparticles in nanofluids and studied flow features. In developing the Lattice Boltzmann equation, they considered buoyance, gravitational, drag, Brownian and interaction forces affecting nanoparticles and the reaction of the Brownian and drag forces acting on fluid molecules. Zhou et al., [38] proposed the Multi-Component Single-component Hybrid Method (MSLM), which applies the Lattice Boltzmann method with different grid sizes and single-phase and two-phase technics in the numerical analysis of nanofluids. The comparisons revealed that the results from the hybrid method are very close to the multi-component lattice Boltzmann method with higher efficiency in computation time consumption. Nabavitabatabayi et al., [41] applied multiple relaxation LBM to study nanofluids' velocity field and heat transfer enhancement in an enclosure with a local heat source. Analysing the simulation results revealed that increasing the Rayleigh number leads to enhanced convective heat transfer by overcoming buoyancy over viscous force. Yang and Lia [42] studied flow features and heat transfer of Al_2O_3-Water nanofluid flow in a microchannel under a laminar regime. Comparing the results with Control Volume Method showed that LBM can predict as accurately as Control Volume Method. Furthermore, they concluded their LBM is only valid in low Reynolds numbers, as the mesh number is small. In the case of higher Reynolds numbers, the mesh number should be more. Abdollahzadeh et al [43] adopted a two-phase Lattice Boltzmann approach to study Al_2O_3 nanofluids in a channel with a low Reynolds number.

The present work studies the hydrothermal behaviour of the laminar forced convection flow of a nanofluid inside a BFS microchannel with constant heat flux from the wall downstream of the step. This work investigates the effects of applying inserts, as turbulators or vortex generators, through the flow stream like square ribs downstream of the step and hemispherical grooves on the top wall of the microchannel to direct flow downward toward the hot surface. To the best of the authors'

Table 2
The thermophysical properties of the employed fluids.

Fluid	ρ (kg/m3)	k (W/m·K)	Cp (J/kg.K)	μ (kg/m.s)
Water	997.0	0.7	4171.0	6.53E-04
Al_2O_3	3880.0	39.2	765.0	–
Al_2O_3-Water	1107.5	0.8	3713.0	7.31E-04

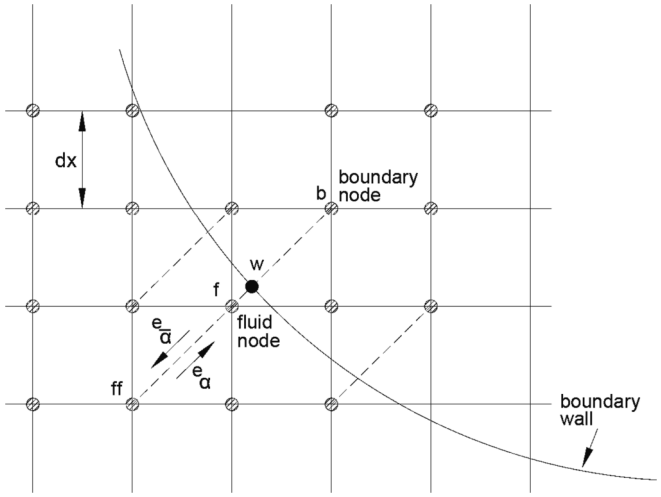

Fig. 2. 2D projection of the layout of the curved wall boundary.

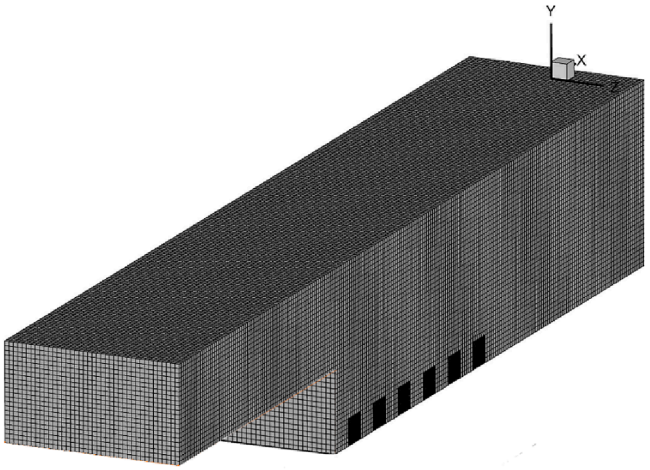

Fig. 3. Generated mesh in the present work for Lattice Boltzmann analysis.

knowledge, this study is the first one with hemispherical grooves applied as turbulators in the BFS microchannel.

Numerical procedure

Model schematics and assumptions

In this study, nanofluid heat transfer and fluid flow in an MBFS considering a three-dimensional, steady state, laminar, single phase, and incompressible model was numerically investigated. Fig. 1 shows the microchannel schematic with geometrical parameters. The values of the geometrical parameters are listed in Table 1. In the preliminary base model, six ribs with square cross-section were added to the bottom wall of the downstream step. As shown in Fig. 1b, the first section of this wall is exposed to a constant heat flux of 28.7 mW/m^2. Also, two side-by-side hemispherical dimples were mounted on the top wall of the

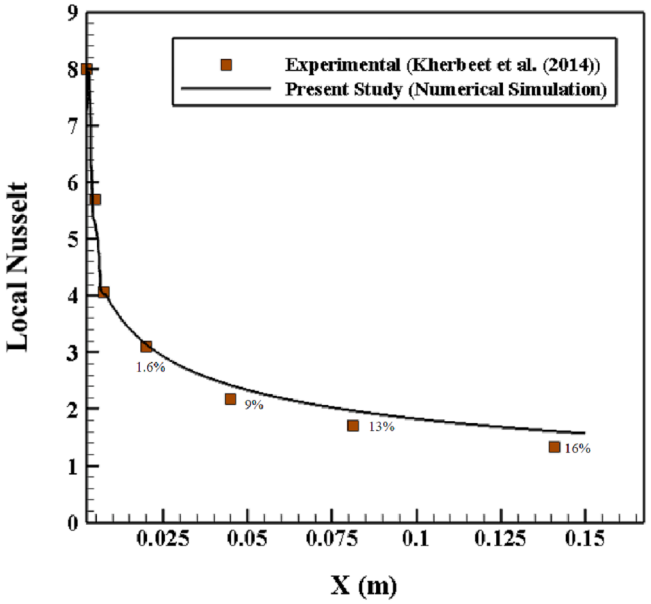

Fig. 4. Comparison of the results of the present numerical study with the experimental results from Kherbeet et al., [61].

microchannel to steer the flow downward close to the surface with constant heat flux. Moreover, 4% Al_2O_3-Water nanofluid was employed as the working fluid, and thermal equilibrium and no-slip condition between Al_2O_3 nanoparticles and water was assumed.

Boundary conditions

In this study, the boundary conditions are set as below:

- The inlet temperature is 25 ℃ (at X = 0, T_i = 25 ℃).
- Inlet velocity is assumed in the range of 0.62—1.54 m/s depending on Reynolds number ranging of Re = 40–100. (X = 0, 0 ≤ Y ≤ 1 and 0 ≤ Z ≤ 1 then u = u_i, v = 0, and r = 0)
- A section of the bottom wall downstream of the step is heated by a constant heat flux of 28.7 MW.m^{-2}, and other wall surfaces are adiabatic. ($T(i.j+1.k) = T(i.j.k) + \frac{q.dx}{k}$)
- No slip condition on the walls (u = 0, v = 0, and r = 0).
- All the microchannel walls are adiabatic except in the constant heat flux section (for instance, at the top wall, Y = 1, 0 ≤ X ≤ 1 and 0 ≤ Z ≤ 1, then $\frac{\delta T}{\delta y} = 0$).
- The extrapolation method is used for outlet temperature and velocity. For instance, at the outlet (X = 1), f_1 (i, j, k) is one of the unknown density distribution functions: $f_1(i,j,k) = 2 \times f_1(i-1.j.k) - f_1(i-2.j.k))$

Physical properties of nanofluid

To calculate nanofluid's properties, a solid–liquid interfacial layer between nanoparticles and base fluid must be considered, as it affects nanofluids' thermal conductivity, density, specific heat capacity etc.

Yu and Choi [47] renovated the conventional Maxwell's model to consider the interfacial layer in the effective thermal conductivity model. By applying the Schwartz et al., [48] effective medium theory, Yu and Choi [47] developed the equivalent nanoparticle thermal conductivity as follows:

$$k_{pe} = \frac{\left[2(1-\nu) + (1+\gamma)^3(1+2\nu)\right]\nu}{-(1-\nu) + (1+\gamma)^3(1+2\nu)} k_p \quad (1)$$

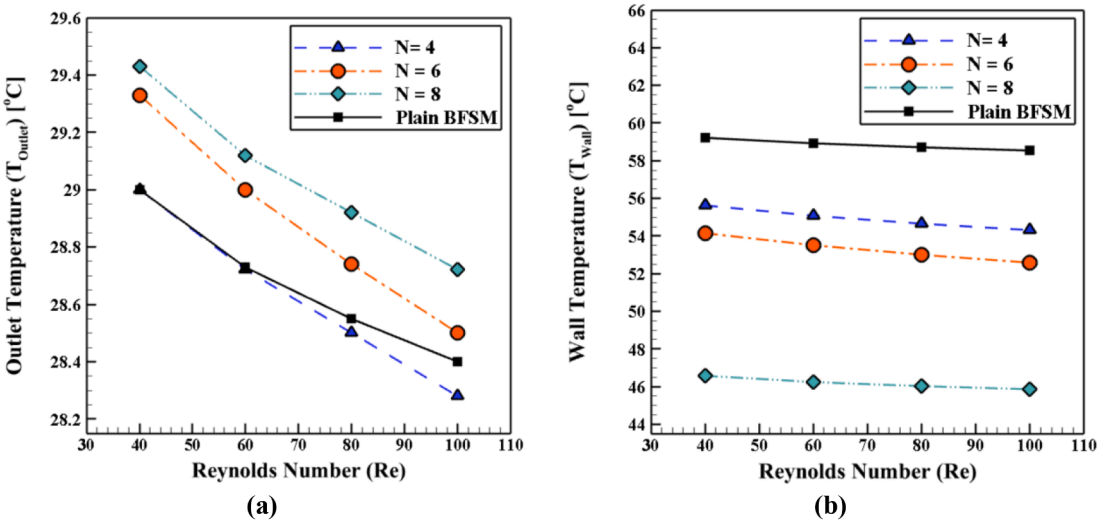

Fig. 5. Effect of the number of ribs on the (a) outlet temperature and (b) wall temperature with constant heat flux at $H_{rb} = H$.

$$\gamma = \frac{t_l}{r_p} \tag{2}$$

$$\nu = \frac{k_l}{k_p} \tag{3}$$

Also assumed,

$$k_l = 10k_f \tag{4}$$

The modified nanofluid's thermal conductivity model is as follows:

$$k_{static} = \frac{k_{pe} + 2k_f + 2\left(k_{pe} - k_f\right)(1+\gamma)^3\varphi}{k_{pe} + 2k_f - \left(k_{pe} - k_f\right)(1+\gamma)^3\varphi}k_f \tag{5}$$

The Brownian motion of nanoparticles is one of the significant factors in the heat transfer enhancement of nanofluids. Hence, Brownian thermal conductivity will be added to static thermal conductivity as presented by Koo and Kleinstreuer [49]:

$$k_{eff} = k_{static} + k_{Brownian} \tag{6}$$

$$k_{Brownian} = 5 \times 10^4 \beta\varphi\rho_f C_{pf}\sqrt{\frac{\mathrm{KT}}{\rho_p \mathrm{d}_p}} f(\mathrm{T}.\varphi) \tag{7}$$

Vajjha and Das [50] modified Koo and Kleinstreuer [49] model using a more comprehensive range of experiments and developed new equations for $f(T, \varphi)$ and β for three different nanoparticles. This new model is valid in temperatures of 298–363 K and 29–77 nm particle size.

$$f(\mathrm{T}.\varphi) = \left(2.8217 \times 10^{-2}\varphi + 3.917 \times 10^{-3}\right)\frac{T}{T_0} + \left(-3.0669 \times 10^{-2}\varphi - 3.91123 \times 10^{-3}\right) \tag{8}$$

$$\beta = 8.4407(100\varphi)^{-1.07304} \tag{9}$$

According to the presented outcomes by Sharifpur et al.[20], it is more accurate to use the following correlation for nanofluid's density:

$$\rho_{nf} = \frac{\varphi\rho_p + (1-\varphi)\rho_f}{(1-\varphi) + \varphi\left(r_p + t_l\right)^3/r_p{}^3} \tag{10}$$

$$t_l = -0.0002833r_p^2 + 0.0475r_p - 0.1417 \tag{11}$$

The study of fluids containing dispersions to understand the rheological behaviour started with Einstein in 1906 [51]. However, this model is valid only for suspensions with a volume concentration of 2% and below [20].

$$\mu_r = \frac{\mu_{nf}}{\mu_f} = (1 + 2.5\varphi) \tag{12}$$

In this study, the Brikman model [52] with equivalent volume concentration will be used for calculating nanofluids' viscosity to account for the solid–liquid interfacial layer:

$$\frac{\mu_{nf}}{\mu_f} = \frac{1}{(1-\varphi_e)^{2.5}} \tag{13}$$

For nanofluid's specific heat capacity, a modified conventional model has been applied; several authors [53–56] used some models as the results from this formula match experimental data.

$$\rho_{nf}c_{p.nf} = \varphi\rho_p c_{p.p} + (1-\varphi)\rho_f c_{p.f} \tag{14}$$

Nanofluid's thermal diffusivity, α and Kinematic viscosity, υ can be calculated using the data from the above equations:

$$\alpha_{nf} = \frac{k_{eff}}{\rho_{nf}c_{p.nf}} \tag{15}$$

$$\vartheta_{nf} = \frac{\mu_{nf}}{\rho_{nf}} \tag{16}$$

Table 2. presents the base fluid, nanoparticle and nanofluid thermophysical properties applied in this work.

Data processing method

The heat transferred to the fluid could be calculated using the below formula:

$$Q = \dot{m}c_{p.nf}(T_{out} - T_{in}) \tag{17}$$

where $\dot{m}$ is the mass flow rate, and T_{in}, and T_{out} are the microchannel inlet and outlet temperatures respectively.

$$q = \frac{Q}{A_w} \tag{18}$$

where q is heat flux, and A_w is the area of a section of the microchannel's bottom wall with constant heat flux. And following equations could be applied to calculate the average heat transfer coefficient and average Nusselt number:

$$h_{ave} = \frac{Q}{A_w(T_w - T_b)} \tag{19}$$

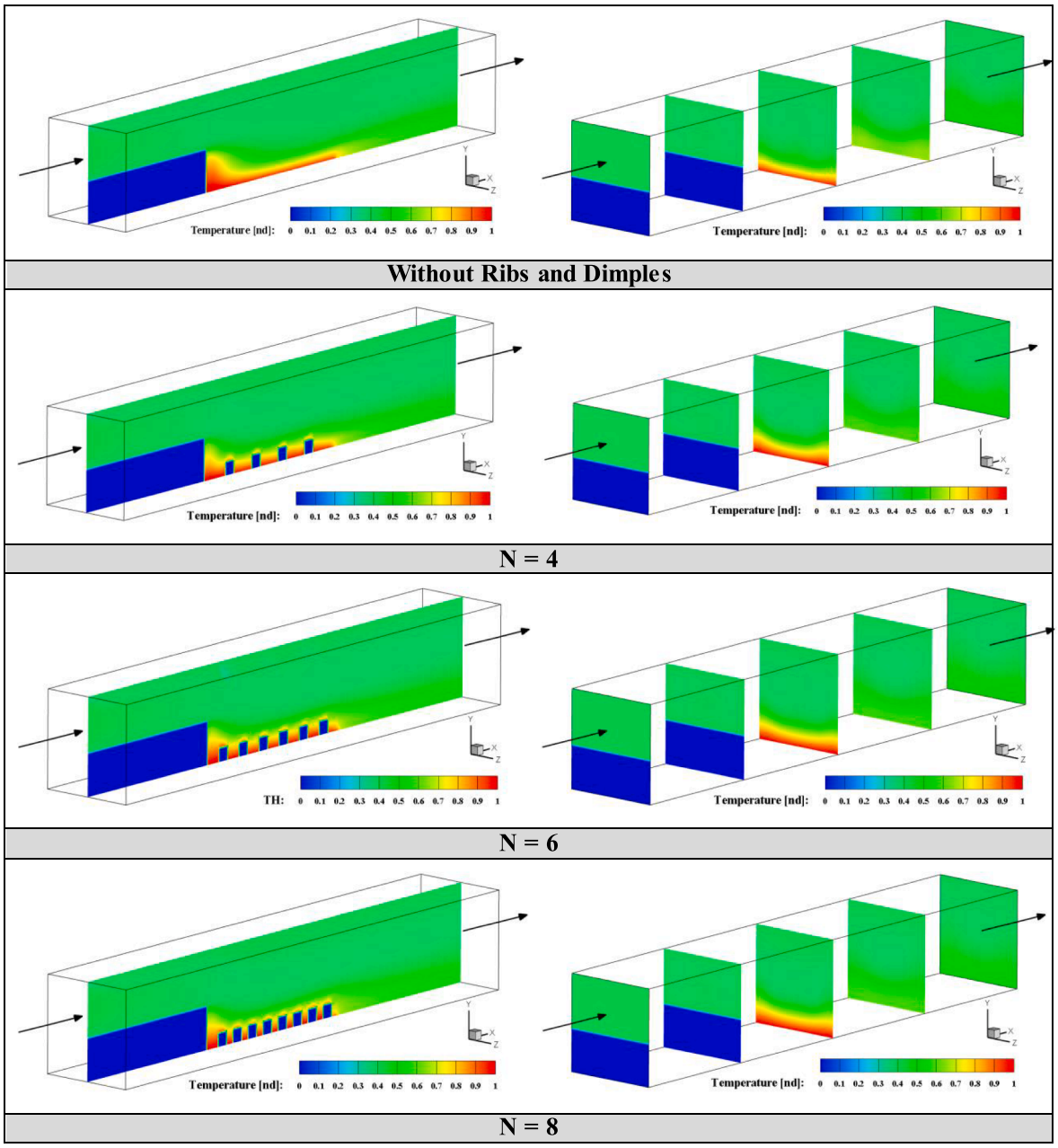

Fig. 6. Contours of temperature distribution in a slice (Z = 0) and various slices in X direction inside the computational domain for various models at Re = 40 and H_{rb} = H.

where T_w is the average temperature of the wall section with constant heat flux, and T_b is the average bulk temperature.

$$Nu_{ave} = \frac{h_{ave} D_h}{k} \tag{20}$$

where D_h is microchannel's hydraulic diameter and k is nanofluids thermal conductivity in average bulk temperature.

Lattice Boltzmann method

There are two different approaches of discrete and continuum in numerical simulations. In the continuum approach, the differential equations of mass, momentum and energy can be solved by defining a finite volume, finite volume, or finite difference scheme and boundary condition. These derived equations are solved on the macroscopic scale by considering boundary and initial conditions to calculate thermo-physical properties.

On the other hand, the discrete approach observes molecules or atoms collisions and identifies the velocity and location of each particle at each time step [30]. Molecular Dynamics (MD) is a microscale method considering each particle's behaviour. Although this microscale method is very convenient in complex geometry, boundary conditions, and multiphase problems, the calculation time and computer resources put some limitations in large systems. Lattice Boltzmann Method operates between two aforementioned macroscopic and microscopic scales, and was generated from Lattice Gas Automata (LGA) method. This method monitors the behaviour of a group of particles instead of individual particles. Particle distribution functions were introduced, which is a definition for the total number of particles in a specific location and time with same specific velocity. To implement LBM, the particle distribution function was introduced, which is a definition for the total number of particles in a particular location and time with the same specific

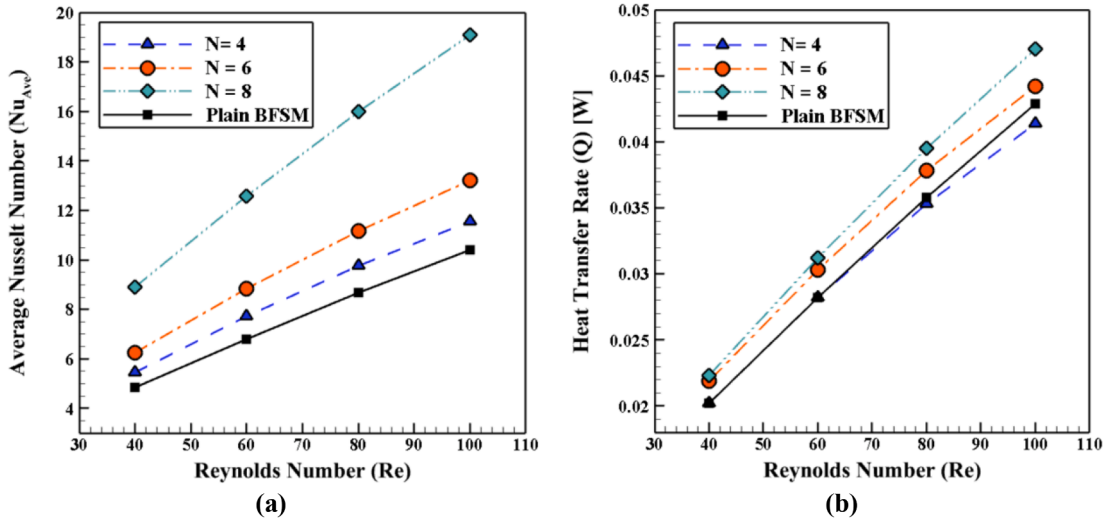

Fig. 7. Effect of the number of ribs on (a) average Nusselt number and (b) heat transfer rate for various Reynolds numbers at $H_{rb} = H$.

velocity, and the changing rate of these distribution functions is named as collision operator.

Boltzmann equation, $f(r,c,t)$, is a statistical equation which describes the number of particles located between r and $r + dr$, with a velocity ranging from c to $c + dc$ at time step dt. The discrete Lattice equation without external force can be written as below in different lattice directions:

$$\frac{\partial f_i}{\partial t} + c_i \nabla f_i = \frac{1}{\tau}(f_i^{eq} - f_i) \tag{21}$$

$$\tau = 3\vartheta \frac{\Delta t}{\Delta x^2} + 0.5 \tag{22}$$

where f^{eq} is the equilibrium distribution function, τ is the relaxation factor, and i is different lattice directions.

The above equation is called the working horse of the Lattice Boltzmann Method by Mohamad [30], like the Navier-Stokes equation in the partial differential approach. The right-hand side of the equation represents the streaming step, and the left-hand side represents the collision step in LBM.

The discretized lattice Boltzmann equation for the flow in circular channel in Pseudo-Cartesian coordinates (x, r) can be written as:

$$f_i(x + c_{ix}\Delta t.r + c_{ir}\Delta t.t + \Delta t) - f_i(x.r.t) = \frac{\Delta t}{\tau}[f_i^{eq}(x.r.t) - f_i(x.r.t)] \tag{23}$$

$$f_i^{eq}(x.r.t) = \omega_i \rho \left[1 + \frac{c_i.\boldsymbol{u}}{c_s^2} + \frac{(c_i.\boldsymbol{u})^2}{2c_s^4} - \frac{u^2}{2c_s^2}\right] \tag{24}$$

where

$$c_s = \frac{c}{\sqrt{3}} \tag{25}$$

$$c = \frac{\Delta x}{\Delta t} \tag{26}$$

Curved boundaries in Lattice Boltzmann method

The curved boundary of hemispherical dimples needs some attention in LBM boundary condition calculations. Most of the studies applying LBM used rectangular geometries, and there is a lake of literature focusing on curved boundaries. In most of the studies with curved boundaries, stairs like geometry was used to model the boundaries in LBM, which this approximation reduces the accuracy of the results [57]. Filippova and Hanel [58] applied grid refinement and boundary fitting methods to ease the Lattice Boltzmann (BGK) in complex geometries. In their study, they've modelled a cylinder perpendicular to the flow path in a channel and for the area close to the boundary of cylinder the lattice been designed finer to observe the changes in more detail in critical areas. The authors explained the LBM accuracy reduction from second order to first order in curved boundaries, so they applied a boundary fitting solution proposed by the same authors [59] for steady-state flows. to overcome the accuracy issue in curved or complicated surfaces. Mei et al., [57] modified the [59] model to get more precise results in curved and complicated boundaries.

Fig. 2 is a two-dimensional projection of the curved wall boundary. Nodes b, f and w demonstrate the solid, fluid and wall nodes, respectively. δx denotes the vertical and horizontal lattice spaces, and Δ is the fraction of the link between solid and fluid nodes as follows:

$$\Delta = \frac{|\boldsymbol{x}_f - \boldsymbol{x}_w|}{|\boldsymbol{x}_f - \boldsymbol{x}_b|} \tag{27}$$

The e_α is the discrete velocity from node f to b, and

$$e_\alpha = -e_{\bar{\alpha}} \tag{28}$$

$$f_{\bar{\alpha}}(\boldsymbol{x}_f = \boldsymbol{x}_b + e_{\bar{\alpha}}\delta t.t + \delta t) = \widetilde{f}_{\bar{\alpha}}(\boldsymbol{x}_b.t) \tag{29}$$

Filippova and Hanel [58] proposed a linear interpolation method as follows:

$$\widetilde{f}_{\bar{\alpha}}(\boldsymbol{x}_b.t) = (1-\chi)\widetilde{f}_\alpha(\boldsymbol{x}_f.t) + \chi f_\alpha^{(*)}(\boldsymbol{x}_b.t) + 2\omega_\alpha \rho \frac{3}{c^2} e_{\bar{\alpha}} u_w \tag{30}$$

$$u_w \equiv u(x_w.t) \tag{31}$$

where u_w is the fluid velocity at the wall boundary, and χ is an indication of the proportions of $\widetilde{f}_\alpha(x_f.t)$ and $f_\alpha^{(*)}(\mathbf{x}_b.t)$ that affects their interpolation or extrapolation for the calculation of $\widetilde{f}_{\bar{\alpha}}(x_b.t)$. $f_\alpha^{(*)}(\mathbf{x}_b.t)$ is a fictitious equilibrium distribution function as follows:

$$f_\alpha^{(*)}(x_b.t) = \omega_\alpha \rho(x_f.t)\left[1 + \frac{3}{c^2} e_\alpha \bullet u_{bf} + \frac{9}{2c^4}(e_\alpha \bullet u_f)^2 - \frac{3}{2c^2} u_f \bullet u_f\right] \tag{32}$$

$$u_f \equiv u(x_f.t) \tag{33}$$

u_f considered as the velocity of the fluid close to the boundary wall.

$$\boldsymbol{u}_{bf} = (\Delta - 1)\boldsymbol{u}_f/\Delta + \boldsymbol{u}_w/\Delta \tag{34}$$

Filippova and Hanel [58] assumed Slow Flow condition and applied Chapman–Enskog expansion to calculate $\widetilde{f}_\alpha(x_f.t)$ as follows:

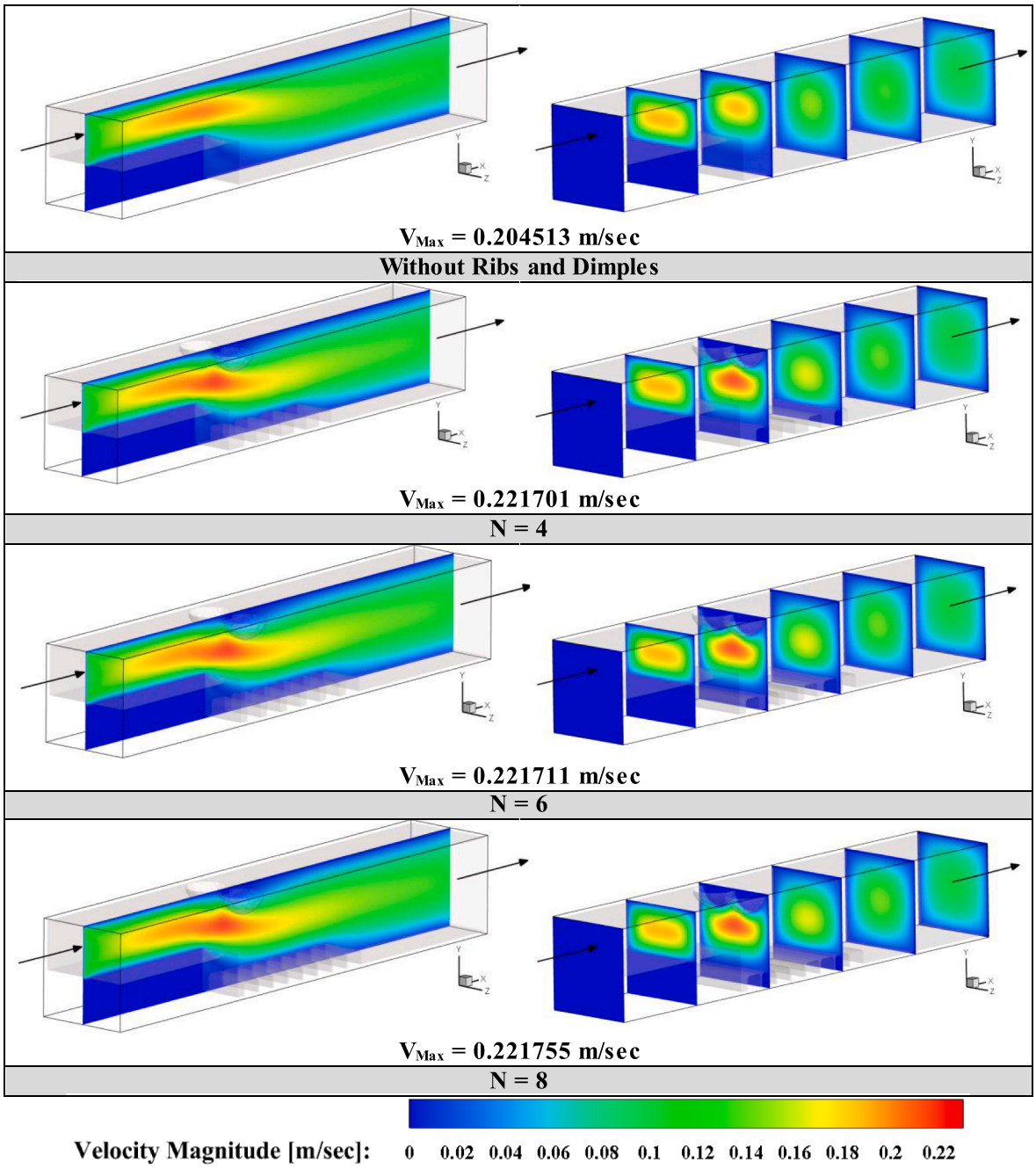

Fig. 8. Contours of velocity magnitude in a slice (Z = 0) and various slices in X direction inside the computational domain for various models at Re = 40 and H_{rb} = H.

$$f_{\bar{\alpha}}(\boldsymbol{x}_f.t) \approx f_{\bar{\alpha}}^{(eq)}(\boldsymbol{x}_f.t) - \lambda e_{\bar{\alpha}} \bullet \nabla f_{\bar{\alpha}}^{(eq)}(\boldsymbol{x}_f.t) \tag{35}$$

$$f_{\bar{\alpha}}^{(eq)}(\boldsymbol{x}_f.t) = \rho w_\alpha \left[1 + \frac{3}{c^2}\boldsymbol{e}_{\bar{\alpha}} \bullet \boldsymbol{u} + \frac{9}{2c^4}(\boldsymbol{e}_{\bar{\alpha}} \bullet \boldsymbol{u})^2 - \frac{3}{2c^2}\boldsymbol{u} \bullet \boldsymbol{u}\right] \tag{36}$$

And $\nabla f_{\bar{\alpha}}^{(eq)}(\boldsymbol{x}_f.t)$ in near incompressible condition could be estimated as below:

$$\nabla f_{\bar{\alpha}}^{(eq)}(\boldsymbol{x}_f, t) = \rho w_\alpha \frac{3}{c^2}\boldsymbol{e}_{\bar{\alpha}} \bullet \nabla \boldsymbol{u} \tag{37}$$

Using the below concept,

$$f_{\bar{\alpha}}^{(eq)}(\boldsymbol{x}_f, t) = f_\alpha^{(eq)}(\boldsymbol{x}_f, t) - 2\rho w_\alpha \frac{3}{c^2}\boldsymbol{u}_f \bullet \boldsymbol{e}_\alpha \tag{38}$$

And substituting Equations (36), (37) and (38) in Equation (35),

$$\begin{aligned} f_{\bar{\alpha}}(\boldsymbol{x}_f, t) &= f_\alpha^{(eq)}(\boldsymbol{x}_f, t) - 2\rho w_\alpha \frac{3}{c^2}\boldsymbol{u}_f \bullet \boldsymbol{e}_\alpha - \tau\delta t 2\rho w_\alpha \frac{3}{c^2}\boldsymbol{e}_\alpha \bullet \nabla \boldsymbol{u} \bullet \boldsymbol{e}_\alpha \nabla f_{\bar{\alpha}}^{(eq)}(\boldsymbol{x}_f, t) \\ &= \rho w_\alpha \frac{3}{c^2}\boldsymbol{e}_{\bar{\alpha}} \bullet \nabla \boldsymbol{u} \end{aligned} \tag{39}$$

where,

$$\lambda = \tau\delta t \tag{40}$$

As per the equilibrium distribution function equation:

$$f_\alpha^{(eq)}(\boldsymbol{x}_f, t) = \rho w_\alpha \left[1 + \frac{3}{c^2}\boldsymbol{e}_\alpha \bullet \boldsymbol{u} + \frac{9}{2c^4}(\boldsymbol{e}_\alpha \bullet \boldsymbol{u})^2 - \frac{3}{2c^2}\boldsymbol{u} \bullet \boldsymbol{u}\right] \tag{41}$$

The $f_\alpha^{(*)}(\mathbf{x}_b, t)$ equation could be re-written as follow:

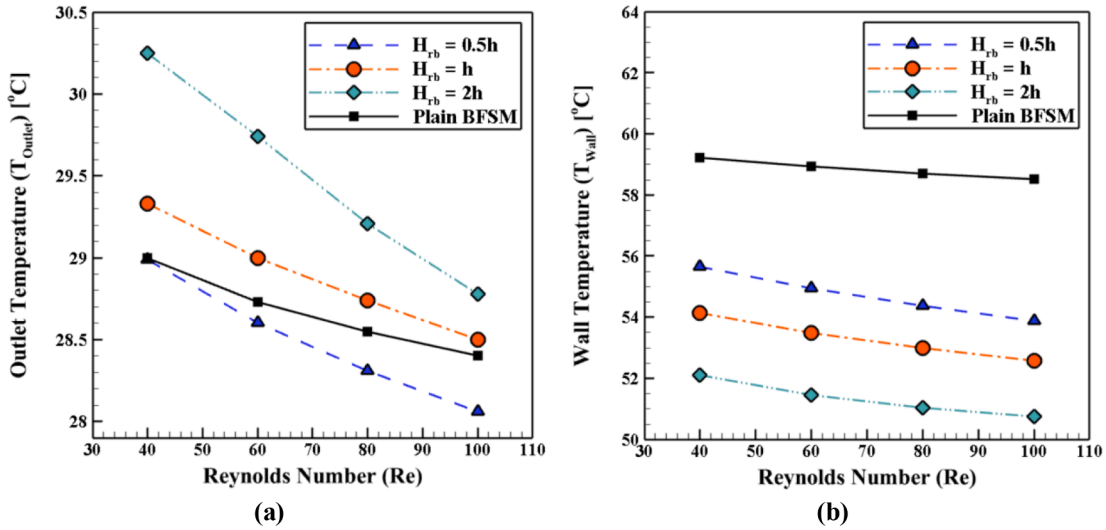

Fig. 9. Effect of the height of the ribs on the (a) outlet temperature and (b) wall temperature with constant heat flux at N = 6.

$$f_\alpha^{(*)}(\mathbf{x}_b,t) = f_\alpha^{(eq)}(\boldsymbol{x}_f,t) + \rho w_\alpha \frac{3}{c^2}\boldsymbol{e}_\alpha \bullet (u_{bf} - u_f) \tag{42}$$

From the above expressions, the $\widetilde{f}_{\bar{\alpha}}(\boldsymbol{x}_b, t)$ can be expressed as:

$$\widetilde{f}_{\bar{\alpha}}(\boldsymbol{x}_b,t) \approx f_\alpha^{(eq)}(\boldsymbol{x}_f,t) + (1-\chi)(1-1/\tau)f\alpha(\boldsymbol{x}_f,t) + w_\alpha\rho\frac{3}{c^2}e_\alpha.(\chi u_{bf} - \chi u_f - 2u_w) = f_\alpha^{(eq)}(\boldsymbol{x}_f,t) - (1-\chi)(\tau-1)\delta t w_\alpha\rho\frac{3}{c^2}e_\alpha.\nabla u.e_\alpha + w_\alpha\rho\frac{3}{c^2}e_\alpha.(\chi u_{bf} - \chi u_f - 2u_w) \tag{43}$$

From Equations (29), (43), and (39):

$$f_\alpha^{(eq)}(\boldsymbol{x}_f,t) - (1-\chi)(\tau-1)\delta t w_\alpha\rho\frac{3}{c^2}e_\alpha.\nabla u.e_\alpha + w_\alpha\rho\frac{3}{c^2}e_\alpha.(\chi u_{bf} - \chi u_f - 2u_w) = f_\alpha^{(eq)}(\boldsymbol{x}_f,t) - 2\rho w_\alpha\frac{3}{c^2}\boldsymbol{u}_f \bullet \boldsymbol{e}_\alpha - \tau\delta t 2\rho w_\alpha\frac{3}{c^2}\boldsymbol{e}_\alpha \bullet \nabla\boldsymbol{u} \bullet \boldsymbol{e}_\alpha \tag{44}$$

In case of $u_{bf} = u_f$:

$$\chi = (2\Delta - 1)/(\tau - 1) \tag{45}$$

and if $u_{bf} = (\Delta - 1)u_f/\Delta + u_w/\Delta$

$$\chi = (2\Delta - 1)/\tau \tag{46}$$

Based on Filippova and Hanel [58] paper, they couldn't find stable results from Equation (45) when Δ is smaller than 1/2, therefor they defined the below criteria:

$$\begin{cases} u_{bf} = \dfrac{(\Delta-1)u_f}{\Delta} + \dfrac{u_w}{\Delta} and \chi = (2\Delta-1)/\tau for \Delta \geq \dfrac{1}{2} \\ u_{bf} = u_f and \chi = (2\Delta-1)/(\tau-1) for \Delta < \dfrac{1}{2} \end{cases} \tag{47}$$

Mei et al., [57] modified the above equation for the boundary nodes with Δ smaller than 1/2.

$$\begin{cases} u_{bf} = \dfrac{(\Delta-1)u_f}{\Delta} + \dfrac{u_w}{\Delta} and \chi = (2\Delta-1)/\tau for \Delta \geq \dfrac{1}{2} \\ u_{bf} = u_f and \chi = (2\Delta-1)/(\tau-2) for \Delta < \dfrac{1}{2} \end{cases} \tag{48}$$

Mei et al., [60] studied the curved boundary condition in LBM and investigated the efficiency and accuracy of 3D LBM models; D_3Q_{15}, D_3Q_{19}, and D_3Q_{27}. Comparing three different 3D methods revealed that the D_3Q_{19} method's accuracy rate is higher than D_3Q_{15} and is more efficient than D_3Q_{27}.

In curved boundaries, they applied Cartesian coordinates with an interpolation technique. As they mentioned, the second-order accuracy in boundary conditions is achievable if the boundary line be considered in the middle of solid and fluid nodes, which means Δ = 0.5;

As shown clearly in Fig. 2, the Δ won't be equal to 0.5 in all boundary nodes because of the curved boundary; they tried to improve the available models, like the one developed by Mei et al., [57], to get more accurate results. They noticed in previous models, the computational accuracy decreases when Δ is closer to 1; for instance, for Δ = 0.87, τ need to be adjusted to 0.6 to get results with the desired accuracy. There is different Δ throughout the boundary in curved boundaries, so they tried to improve the available models for higher accuracy in a wider range.

$$u_{bf} = \left[1 - \frac{3}{2\Delta}\right]u_f + \frac{3}{2\Delta}u_w and \chi = (2\Delta-1)/(\tau+1/2) for \Delta \geq \frac{1}{2} \tag{49}$$

Grid independency study and validation

Applying a Core i7, 2.2 GHz with 8 GB of RAM PC, a homemade 3D FORTRAN code is developed and run to perform the numerical study on 4% Al_2O_3-Water nanofluid through a backward-facing microchannel. To ensure grid independency, four grids with the different number of the cell were considered; including 20 × 20 × 112, 30 × 30 × 168, 40 × 40 × 224, and 50 × 50 × 280. Nanofluid outlet temperature, T_{out}, and heat transferred, Q, were chosen to be compared in these four grids. Accordingly, it was obtained that the differences between the results of grids 40 × 40 × 224 and 50 × 50 × 280 were not significant. So, the grid with 40 × 40 × 224 number of cells was applied for this study's numerical studies. Fig. 3 presents the generated grid for this study (40 × 40 × 224).

To validate the present numerical study, the distribution of the local

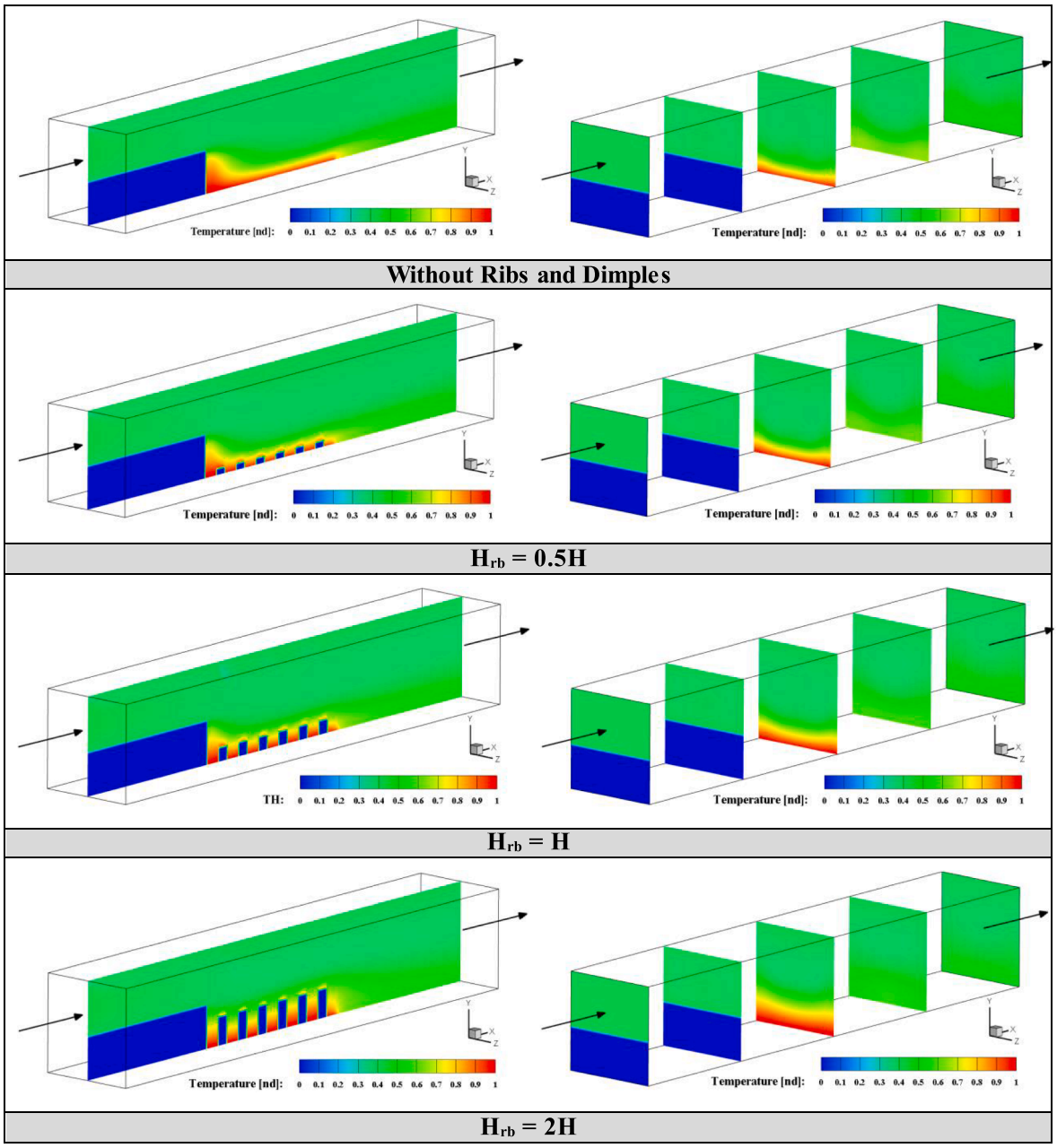

Fig. 10. Contours of temperature distribution in a slice (Z = 0) and various slices in X direction inside the computational domain for various models at Re = 40 and N = 6.

Nusselt number of the plain MBFS (without any turbulator or insert) is compared with the Kherbeet et al., [61] experimental results. As demonstrated in Fig. 4, the results from this study are in acceptable agreement with experimental data. The percentage differences are shown on the graph and are insignificant, which could result from uncertainties and heat dissipations in the experimental process.

Results and discussions

A nanofluid of 47 nm Al_2O_3 nanoparticles dispersed in water with a volume fraction of 4% is employed as the working fluid. At the inlet, a velocity of 0.62—–1.54 m/s depending on Reynolds number ranging of Re = 40–100 and a constant temperature of 25 ℃ are assumed. To study the heat transfer behaviour of nanofluid in different cases, the average Nusselt number, microchannel outlet average temperature, and the average temperature of the wall with constant heat flux were derived from the developed homemade LBM code results. It should be noted that in the present work, the geometrical factors of the dimples were kept constant.

The impact of the number of ribs (N)

In the present section, the influence of the number of ribs on the hydrothermal behaviour of nanofluid flow inside the proposed microscale backward-facing step was evaluated numerically. The number of dimples placed at the considered channel was kept constant by two. Also, the height of the ribs was kept constant by H_{rb} = H. The influence of the number of ribs on the outlet temperature and wall temperature with constant heat flux at H_{rb} = H are demonstrated in Fig. 5a and 5b, respectively.

Fig. 5a illustrates that the outlet temperature declines as the Reynolds number rises. This trend is recorded in all considered cases with

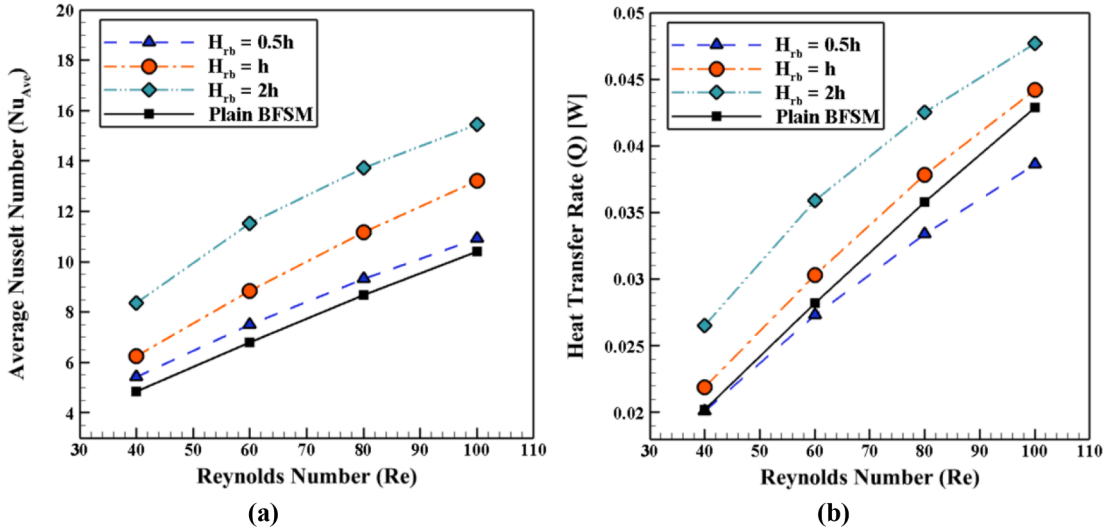

Fig. 11. Effect of Ribs Height on the (a) average Nusselt number and (b) heat transfer rate for various models at N = 6.

the various number of ribs as well as the case without ribs and dimples as plain MBFS. Moreover, it can be observed that the highest outlet temperature belongs to the case with eight ribs at all considered Reynolds numbers. However, for the minimum outlet temperature, it should be noted that at lower Reynolds numbers (Re = 40 and 60), the differences between the case with four ribs and plain MBFS are low. Increasing the Reynolds number (Re = 80 and 100) makes the outlet temperature difference between these two cases appear. The differences between these cases augments by Reynolds number, and consequently, it can be concluded that the minimum outlet temperature belongs to the case with ribs at the highest considered Reynolds number, Re = 100.

Fig. 5b indicates that by increasing the Reynolds number, the wall temperature decreases; however, the slopes of these profiles are significantly lower than the plotted profiles in Fig. 5a. Profiles of wall temperature for various cases and Reynolds numbers show that in all considered cases (with dimples and ribs) and Reynolds numbers, the wall temperature is lower than the case with plain MBFS. In other words, employing the proposed inserts (dimples and ribs) leads to lower wall temperature and consequently improved wall (with constant heat flux) cooling or heat transfer rate (between the hot wall and nanofluid flow) compared to the plain MBFS (without any inserts).

The contours of temperature distributions are shown to demonstrate the impact of using proposed inserts on the thermal behavior of nanofluid. Accordingly, Fig. 6 shows heat transfer contours at Re = 40 and H_{rb} = H. It can be concluded that employing ribs leads to higher disturbance on the hot wall with constant heat flux, and consequently, enhanced heat transfers between the hot wall and nanofluid flow. The effect of the number of ribs on the average Nusselt number and heat transfer rate at H_{rb} = H are presented in Fig. 7a and 7b, respectively. Fig. 7a illustrates that the higher the Reynolds number, the larger the average Nusselt number; this trend can be appreciated in all cases. Furthermore, it can be seen that the average Nusselt number of all cases is higher than the plain MBFS in all Reynolds numbers, which depicts the positive effect of employing ribs with any number (in the studied range).

Furthermore, according to Fig. 7a, it can be concluded that at a constant Reynolds number, augmentation of the number of ribs leads to a higher average Nusselt number. Moreover, it should be noted that the differences between the cases rise as the Reynolds number increases. At the lowest evaluated Reynolds number (Re = 40), the average Nusselt number of the cases N = 4, 6, and 8 is more than the case with plain MBFS by about 10, 20, and 80%. At the highest considered Reynolds number (Re = 100), the average Nusselt number of the cases N = 4, 6, and 8 is greater than the case with plain MBFS by about 9.52%, 26.67%, and 81.9%. For instance, at Re = 40, as the number of ribs rises from N = 4 to N = 8 (100% growth), the average Nusselt number augments by about 63.64%. Moreover, at Re = 100, increasing the number of ribs by 100% (from N = 4 to N = 8) causes an increase in the average Nusselt number by about 64.65%.

Fig. 7b illustrates that similar to the trend of Fig. 7a, the heat transfer rate rises as the Reynolds number increases. Also, it can be seen that except for the cases N = 4, the heat transfer rate of all cases is more than the plain MBFC. The differences between the cases N = 6 and N = 8 are insignificant at a lower Reynolds number and raised at a higher Reynolds number. Concerning the N = 4, it can result that adding ribs with the number of four does not enhance the heat transfer rate.

Fig. 8 demonstrates the contours of velocity magnitude at Re = 40 and H_{rb} = H. The contours show that applying ribs leads to higher velocity magnitude because employing ribs causes reduced fluid passage cross-section and, consequently, more incredible maximum velocity according to the continuity equation.

The impact of the height of the ribs (H)

In this section, the impact of the height of the ribs on the hydrothermal behaviour of nanofluid flow inside the proposed microscale backward-facing step was investigated by performing numerical simulations. Similar to ***Section 4.1***, the number of dimples placed at the considered channel was kept constant. Furthermore, the number of ribs was kept constant by N = 6. The effect of the height of ribs on the outlet temperature and temperature of the wall with constant heat flux at N = 6 are presented in Fig. 9a and 9b, respectively.

Fig. 9a shows as the Reynolds number increases, the outlet temperature drops and this trend was verified in all considered cases with various heights of the ribs in addition to the case without rib and dimple as plain MBFS. Furthermore, it can be seen that at all considered Reynolds numbers, the maximum outlet temperature belongs to the case with H_{rb} = 2H. But, for the lowest outlet temperature, it should be noted that at the lowest considered Reynolds number (Re = 40), the difference between the cases H_{rb} = 0.5H and plain MBFS is low, and at these Reynolds numbers, the lowest outlet temperature belongs to two cases; H_{rb} = 0.5H and plain MBFS. Also, as the Reynolds number rises, the differences between the cases H_{rb} = 0.5H and plain MBFS appear, and at Re = 100, employing ribs with N = 6 and H_{rb} = 0.5H leads to a decrease in the outlet temperature by about 1.6%. In other words, generally, among the considered cases, the minimum outlet temperature belongs to the case with H_{rb} = 0.5H. It means that employing ribs without considering the suitable geometrical parameters will not result in a better heat transfer rate than the plain channel.

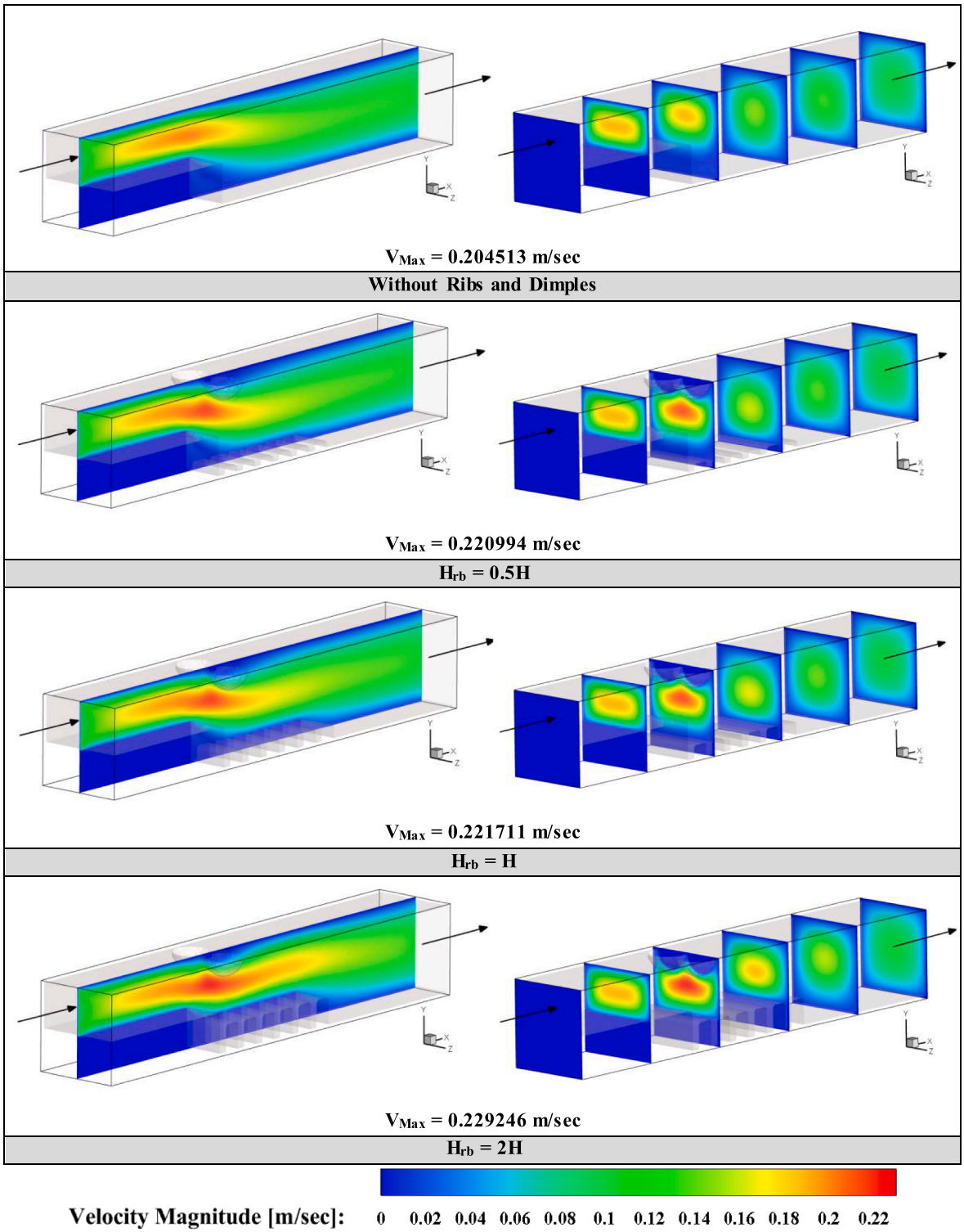

Fig. 12. Contours of temperature distribution in a slice (Z = 0) and various slices in X direction inside the computational domain for various models at Re = 40 and N = 6.

Fig. 9b shows that by growing the Reynolds number, the wall temperature reduces; however, the slopes of these profiles are lower than the plotted profiles in Fig. 9b expressively. Profiles of wall temperature for different models and Reynolds numbers prove that in all considered models (with dimples and ribs) and Reynolds numbers, the wall temperature is lower than the model with plain MBFS. In other words, employing the proposed inserted (dimples and ribs) leads to lower wall temperature and consequently improved wall (with constant heat flux) cooling or heat transfer rate (between the hot wall and nanofluid flow) compared to the plain MBFS (without any inserts).

Accordingly, Fig. 10 demonstrates the heat transfer contour for the case with six ribs and Re = 40. It can be concluded that employing ribs leads to more disturbance on the hot wall with constant heat flux and, consequently, more heat transfers between the hot wall and nanofluid flow.

The influence of the height of the ribs on the average Nusselt number

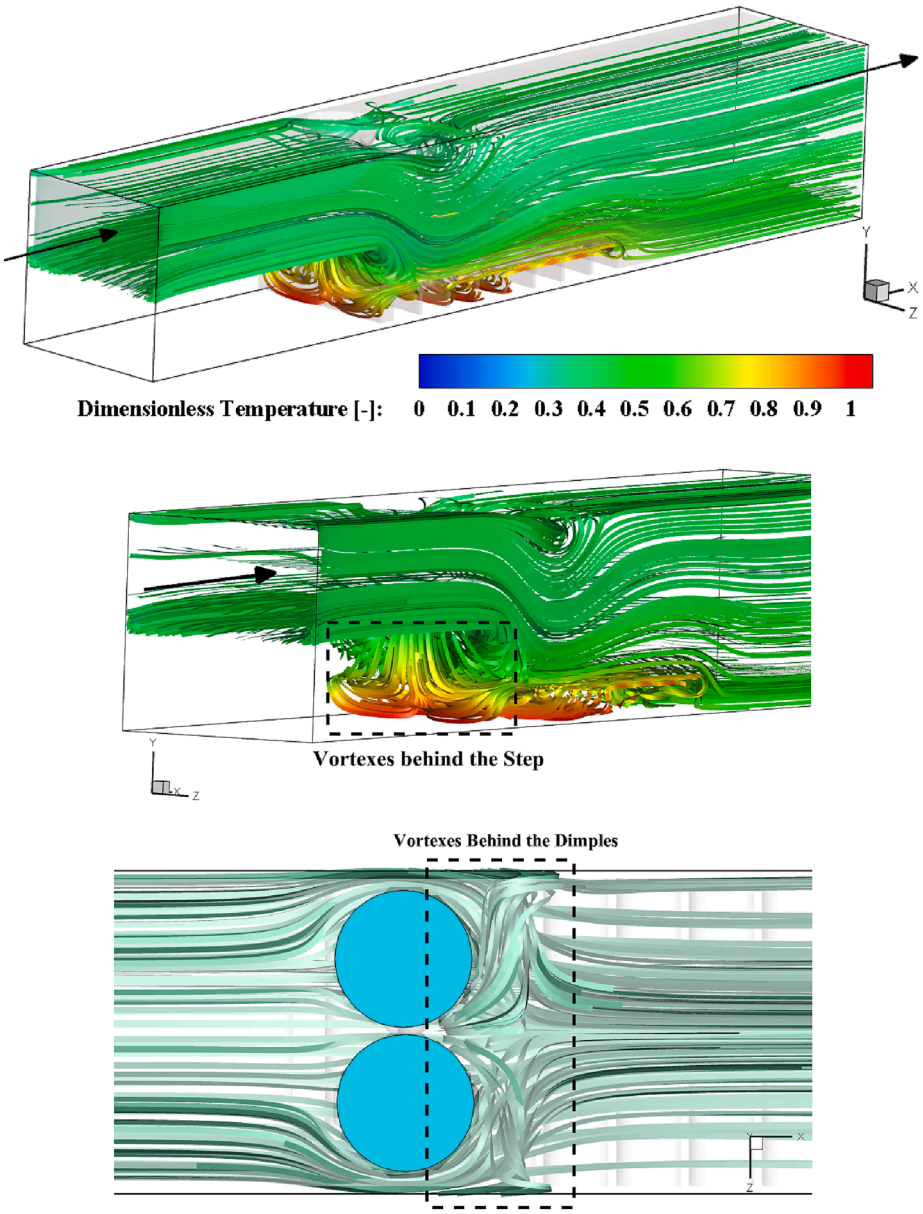

Fig. 13. Flow Streamlines at Re = 40 and various views.

and heat transfer rate at N = 6 are shown in Fig. 11a and 11b, respectively. Fig. 11a shows that the more Reynolds number, the more average Nusselt number and this trend can be appreciated in all cases. Furthermore, it can be realized that the average Nusselt number of all cases is higher than the plain MBFS in all Reynolds numbers, which depicts the positive effect of employing ribs with any height (in the studied range).

Moreover, according to Fig. 11a, it can be concluded that at a constant Reynolds number, augmentation of the height of the ribs leads to a more significant average Nusselt number. Furthermore, it should be noted that the differences between the cases increase as the height of the ribs rises. At the lowest evaluated Reynolds number (Re = 40), the average Nusselt number of the cases $H_{rb} = 0.5H$, $H_{rb} = H$, and $H_{rb} = 2H$ is more than the case with plain MBFS by about 10, 26, and 70%. At the maximum considered Reynolds number (Re = 100), the average Nusselt number of the cases $H_{rb} = 0.5H$, $H_{rb} = H$, and $H_{rb} = 2H$ is more than the case with plain MBFS by about 5.77, 27.88, and 49.04%. For example, at Re = 40, as the height of the ribs increases from $H_{rb} = 0.5H$ to $H_{rb} = 2H$ (300% growth), the average Nusselt number augments by about 54.54%. Furthermore, at Re = 100, growing the height of the ribs by 300% (from $H_{rb} = 0.5H$ to $H_{rb} = 2H$) leads to a rise in the average Nusselt number by about 40.91%.

Fig. 11b shows that similar to the trend of the presented outcomes displayed in Fig. 11a, the heat transfer rate increases as the Reynolds number rises. Also, it can be seen that except for the cases $H_{rb} = 0.5H$, the heat transfer rate of all cases is higher than the plain MBFC. The differences between the cases of plain MBFC and $H_{rb} = 0.5H$ are insignificant at lower Reynolds numbers, and this difference grows with increasing Reynolds number.

Concerning the case $H_{rb} = 0.5H$, it can be concluded that employing ribs with a height of 0.5H may not lead to the enhanced heat transfer rate. In other words, among various cases here, the lowest heat transfer rate belongs to the case with $H_{rb} = 0.5H$.

Fig. 12 demonstrates fluid velocity contours at Re = 40 and N = 6. Studying these velocity contours reveals that by increasing the height of the ribs, the fluid passage cross-section decline and consequently, the velocity magnitude rises. Besides, the maximum velocity magnitude of cases $H_{rb} = H$, $H_{rb} = 0.5H$, and $H_{rb} = 2H$ is more than the case with plain MBFC by about 8.06, 8.41, and 12.09%, respectively.

Fig. 13 shows the streamlines in the backward-facing step microchannel at Re = 40. The vortexes generated behind the step, between ribs and behind hemispherical dimples are clearly visible, confirming the advantages of inserting the step, ribs and dimples in microchannels for enhanced heat transfer performance. As it's been presented in this section, inserting ribs to the bottom wall of the microchannel leads to vortex creation between ribs. Consequently, it disrupts the temperature boundary layer, hence higher heat transfer. Also, adding hemispherical grooves on the top wall directs the flow toward the heated wall, leading to higher heat transfer in the channel.

Conclusion

This research studied the hydraulic and heat transfer behaviours of laminar forced convection flow of a nanofluid in a BFS microchannel equipped with dimples on the top surface and ribs on the bottom surface as turbulators. Hemispherical grooved as dimples were added to the top wall. A three-dimensional thermal LBM was applied to study heat transfer and flow behaviour of the laminar flow of 4% concentration of Al_2O_3-water nanofluid in Reynolds numbers ranging between 40 and 100 through the MBFS. The summaries of the results are as follows:

- Increasing the number or the height of ribs improves heat transfer in the backward-facing step microchannels.
- At a constant Reynolds number, augmentation of the number of ribs leads to a higher average Nusselt number.
- At the lowest evaluated Reynolds number (Re = 40), the average Nusselt number of the cases N = 4, 6, and 8 is more than the case with plain MBFS by about 10, 20, and 80%. At the highest considered Reynolds number (Re = 100), the average Nusselt number of the cases N = 4, 6, and 8 is greater than the case with plain MBFS by about 9.52, 26.67, and 81.9%
- At Re = 40, as the number of ribs rises from N = 4 to N = 8 (100% growth), the average Nusselt number augments by about 63.64%. Moreover, at Re = 100, increasing the number of ribs by 100% (from N = 4 to N = 8) enhance the average Nusselt number by about 64.65%.
- At a constant Reynolds number, augmentation of the height of the ribs leads to a greater average Nusselt number.
- At the lowest evaluated Re number (Re = 40), the average Nusselt number of the cases $H_{rb} = 0.5H$, $H_{rb} = H$, and $H_{rb} = 2H$ is higher than the case with plain MBFS by about 10, 26, and 70%. At the maximum considered Reynolds number (Re = 100), the average Nusselt number of the cases $H_{rb} = 0.5H$, $H_{rb} = H$, and $H_{rb} = 2H$ is higher than the case with plain MBFS by about 5.77, 27.88, and 49.04%
- At Re = 40, as the height of the ribs increases from $H_{rb} = 0.5H$ to $H_{rb} = 2H$ (300% growth), the average Nusselt number augments by about 54.54%. Furthermore, at Re = 100, growing the height of the ribs by 300% (from $H_{rb} = 0.5H$ to $H_{rb} = 2H$) enhances the average Nusselt number by about 40.91%.
- In some cases, with the lower number of ribs or the ones with short ribs, the benefits of applying ribs are negligible or even have adverse effects in some Re numbers.

In the present work, the combination of three different methods to improve the heat transfer rate, including the use of (i) ribs, (ii) dimples, and (iii) nanofluids in the backward-facing step microchannel, was considered, and the hydrothermal behaviour of nanofluid flow was numerically investigated. The examined geometrical parameters were related to the ribs, and the geometrical factors related to the dimple were considered fixed. So, a comprehensive study on the effects of the hemispherical dimples' number, size, and location could be conducted in future work.

CRediT authorship contribution statement

Saboura Yousefi: Conceptualization, Methodology, Investigation, Writing – original draft. **Mostafa Mahdavi:** Supervision. **Seyed Soheil Mousavi Ajarostaghi:** Conceptualization, Investigation, Visualization. **Mohsen Sharifpur:** Supervision.

Declaration of Competing Interest

The authors declare that they have no known competing financial interests or personal relationships that could have appeared to influence the work reported in this paper.

Data availability

No data was used for the research described in the article.

References

[1] D. Lelea, C. Nisulescu, The micro-tube heat transfer and fluid flow of water based Al2O3 nanofluid with viscous dissipation, Int. Commun. Heat Mass Transfer 38 (6) (2011) 704–710.
[2] B. Salman, B. Mohammed, A. Kherbeet, Heat transfer enhancement of nanofluids flow in microtube with constant heat flux, Int. Commun. Heat Mass Transfer 39 (2012) 1195–1204.
[3] A. Karimipour, A. Hossein Nezhad, A. 'Orazio, M. Hemmat Esfe, M.R. Safaei, E. Shirani, Simulation of copper–water nanofluid in a microchannel in slip flow regime using the lattice Boltzmann method, Euro. J. Mech. B Fluids 49 (2015) 89–99.
[4] A. Karimipour, New correlation for Nusselt number of nanofluid with Ag / Al2O3 / Cu nanoparticles in a microchannel considering slip velocity and temperature jump by using lattice Boltzmann method, Int. J. Therm. Sci. 91 (2015) 146–156.
[5] N. Haziq Naqiuddin, L. Huat Saw, M. Chian Yew, F. Yusof, T., Ching Ng, Overview of micro-channel design for high heat flux application, Renew. Sustain. Energy Rev. 82 (2018) 901–914.
[6] A. Ijam, R. Saidur, Nanofluid as a coolant for electronic devices (cooling of electronic devices), Appl. Therm. Eng. 32 (2012) 76–82.
[7] R. Smyth, Measurment in plane separated flow, Letters In Heat And Mass Transfer 2 (1975) 505–514.
[8] B.F. Armaly, F. Dursts, J.C.F. Pereira, Experimental and theoretical investigation of backward-facing step flow, J. Fluid Mech. 127 (1983) 473–496.
[9] T. Lee, D. Mateescu, Experimental and numerical investigation of 2-d backward facing step flow, J. Fluids Struct. 12 (1998) 703–716.
[10] T. Johnson, P. Joubert, The influence of vortex generators on the drag and heat transfer from a circular cylinder normal to an airstream, J. Heat Transfer 91 (1969) 91–99.
[11] P. Yeung, S. Kot, On body-fitted co-ordinates for separated laminar flows past wall-mounted obstacles, Int. J. Numer. Meth. Eng. 21 (1985) 929–939.
[12] C.K. Chen, T.S. Yen, Y.T. Yang, Lattice Boltzmann method simulation of a cylinder in the backward-facing step flow with the field synergy principle, Int. J. Therm. Sci. 45 (2006) 982–989.
[13] F. Selimefendigil, H.F. Öztop, Numerical study of forced convection of nanofluid flow over a backward facing step with a corrugated bottom wall in the presence of different shaped obstacles, Heat Transfer Eng. 37 (15) (2016) 1280–1292.
[14] A.A.R. Alkumait, M. Haj Zaidan, T.K. Ibrahim, Numerical investigation of forced convection flow over backward facing step affected by a baffle position, Journal of Advanced Research in Fluid Mechanics and Thermal Sciences 52 (2018) 33–45.
[15] H.E. Ahmed, A. Kherbeet, M. Ahmed, B. Salman, Heat transfer enhancement of micro-scale backward-facing step channel by using turbulators, Int. J. Heat Mass Transf. 126 (2018) 963–973.
[16] Y. Ma, R. Mohebbi, M.M. Rashidi, Z. Yang, Y. Fang, Baffle and geometry effects on nanofluid forced convection over forward- and backward-facing steps channel by means of lattice Boltzmann method, Phys. A 554 (2020), 124696.
[17] H. Hajji, L. Kolsi, F. Askri, C. Maatki, W. Hassen, M.N. Borjini, Heat transfer and flow structure through a backward and forward-facing step micro-channels equipped with obstacles, Therm. Sci. 25 (2021) 2483–2492.
[18] A.R. Abu Talib, A.K. Hilo, Fluid flow and heat transfer over corrugated backward facing step channel. Case studies, Therm. Eng. 24 (2021), 100862.
[19] R. Ekiciler, M.S.A. Çetinkaya, A comparative heat transfer study between monotype and hybrid nanofluid in a duct with various shapes of ribs, Thermal Science and Engineering Progress 23 (2021), 100913.
[20] M. Sharifpur, S. Yousefi, J.P. Meyer, A new model for density of nanofluids including nanolayer, International Communicat, ions in Heat and Mass Transfer 78 (2016) 168–174.
[21] S. Choi, Enhancing thermal conductivity of fluids with nanoparticles, Development and Applications of Non-Newtonian Flows (1995) 99–105.
[22] M. Sharifpur, T. Ntumba, Parametric analysis of effective thermal conductivity models for nanofluids. in Proceedings of the the ASME 2012 International Mechanical Engineering Congress & Exposition, Houston, (2012).

[23] J. Meyer, P. Nwosu, M. Sharifpur, T. Ntumba, Parametric analysis of effective viscosity models for nanofluids. in Proceedings of the the ASME 2012 International Mechanical Engineering Congress & Exposition, Houston (2012).
[24] S.P. Jang, S.U. Choi, Cooling performance of a microchannel heat sink with nanofluids, Appl. Therm. Eng. 26 (2006) 2457–2463.
[25] E. Abu-Nada, The effect of step height of microscale backward-facing step on mixed convection nanofluid flow and heat transfer characteristics, Int. J. Heat Fluid Flow 29 (2008) 242–249.
[26] A. Kherbeet, H. Mohammed, K. Munisamy, B. Salman, The effect of step height of microscale backward-facing step on mixed convection nanofluid flow and heat transfer, Int. J. Heat Mass Transf. 68 (2014) 554–566.
[27] S. Salman, A. Abu Talib, S. Saadon, M., Hameed Sultan, Hybrid nanofluid flow and heat transfer over backward and forward steps, a review, Powder Technol. 363 (2020) 448–472.
[28] D. Yang, B. Sun, T. Xu, B. Liu, H. Li, Experimental and numerical study on the flow and heat transfer characteristic of nanofluid in the recirculation zone of backward-facing step microchannels, Appl. Therm. Eng. 199 (2021), 117527.
[29] R. Ekiciler, Efects of novel hybrid nanofuid (TiO2–Cu EG) and geometrical parameters of triangular rib mounted in a duct on heat transfer and fow characteristics, J. Therm. Anal. Calorim. 143 (2021) 1371–1387.
[30] A.A. Mohamad, Lattice Boltzmann Method, Springer, Calgary, 2011.
[31] S.S.M. Ajarostaghi, M.A. Delavar, S. Poncet, Thermal mixing, cooling and entropy generation in a micromixer with a porous zone by the lattice Boltzmann method, J. Therm. Anal. Calorim. 140 (2020) 1321–1339.
[32] A. Masoud Ali, M. Angelino, A. Rona, Physically consistent implementation of the mixture model for modelling nanofluid conjugate heat transfer in minichannel heat sinks, Appl. Sci. 12 (2022) 7011.
[33] M. Lappa, S. Inam, Large eddy simulation of three-dimensional hybrid forced-buoyancy convection in channels with a step, Int. J. Heat Mass Transf. 202 (2023), 123767.
[34] L. Chen, K. Asai, T. Nonomura, G. Xi, T. Liu, A review of Backward-Facing Step (BFS) flow mechanisms, heat transfer and control, Thermal Science and Engineering Progress 6 (2018) 194–216.
[35] X. Shan, H. Chen, Lattice Boltzmann model for simulating flows with multiple phases and components, Phys Rev E 47 (1993) 1815–1819.
[36] A. Rahimi, A. Kasaeipoor, E. Hasani Malekshah, M. Paliziand, L. Kolsi, Lattice Boltzmann numerical method for natural convection and entropy generation in cavity with refrigerant rigid body filled with DWCNTs-water nanofluid-experimental thermo-physical properties, Thermal Science and Engineering Progress 5 (2018) 372–387.
[37] Y. Xuan, Z. Yao, Lattice Boltzmann model for nanofluids, Heat Mass Transfer 41 (2005) 199–205.
[38] L. Zhou, Y. Xuan, Q. Li, Multiscale simulation of flow and heat transfer of nanofluid with lattice Boltzmann method, Int. J. Multiph. Flow 36 (2010) 364–374.
[39] H. Nemati, M. Farhadi, K. Sedighi, E. Fattahi, A. Darzi, Lattice Boltzmann simulation of nanofluid in lid-driven cavity, Int. Commun. Heat Mass Transfer 37 (2010) 1528–1534.
[40] G. Kefayati, S. Hosseinizadeh, M. Gorji, H. Sajjadi, Lattice Boltzmann simulation of natural convection in tall enclosures using water/SiO2 nanofluid, Int. Commun. Heat Mass Transfer 38 (2011) 798–805.
[41] M. Nabavitabatabayi, E. Shirani, M.H. Rahimian, Investigation of heat transfer enhancement in an enclosure filled with nanofluids using multiple relaxation time lattice Boltzmann modeling, Int. Commun. Heat Mass Transfer 38 (2011) 128–138.
[42] Y.T. Yang, F.H. Lai, Lattice Boltzmann simulation of heat transfer and fluid flow in a microchannel with nanofluids, Heat Mass Transfer 47 (2011) 1229–1240.
[43] Y. Abdollahzadeh, M. Mehrpooya, S.M.A. Mousavian, H. Moqtaderi, Modeling and simulation of nanofluid in low Reynolds numbers using two-phase Lattice Boltzmann method based on mixture model, Chem. Eng. Res. Des. 192 (2023) 402–411.
[44] A. Rahimi, M. Rahjoo, S.S. Hashemi, M.R. Sarlak, M. Hasani Malekshah, E. Hasani Malekshah, Combination of Dual-MRT lattice Boltzmann method with experimental observations during free convection in enclosure filled with MWCNT-MgO/Water hybrid nanofluid, Therm. Sci. Eng. Progress 5 (2018) 422–436.
[45] N.A.C. Sidik, M. Khakbaz, L. Jahanshaloo, S. Samion, A.N. Darus, Simulation of forced convection in a channel with nanofluid by the lattice Boltzmann method, Nanoscale Res. Lett. 8 (2013) 178.
[46] S.S. Mousavi Ajarostaghi, S. Poncet, Thermal mixing in T-shaped micromixers with a porous block by the lattice Boltzmann method: Influence of the mixing channel configuration, Front. Therm. Eng. (2022).
[47] W. Yu, S. Choi, The role of interfacial layers in the enhanced thermal conductivity of nanofluids A renovated Maxwell mode, J. Nanopart. Res. 5 (2003) 167–171.
[48] L. Schwartz, E. Garboczi, D. Bentz, Interfacial transport in porous media, Application to DC electrical conductivity of mortars, J. Appl. Phys. 78 (10) (1995) 5898–5908.
[49] J. Koo, C. Kleinstreuer, Laminar nanofluid flow in microheat-sinks, Int. J. Heat Mass Transf. 48 (13) (2005) 2652–2661.
[50] R.S. Vajjha, D.K. Das, Experimental determination of thermal conductivity of three nanofluids and development of new correlations, Int. J. Heat Mass Transf. 52 (2009) 4675–4682.
[51] C.T. Nguyen, F. Desgranges, N. Galanis, G. Roy, T. Maré, S. Boucher, H. Angue Mintsa, Viscosity data for Al2O3–water nanofluid—hysteresis is heat transfer enhancement using nanofluids reliable? Int. J. Therm. Sci. 47 (2) (2008) 103–111.
[52] H. Brikman, The viscosity of concentrated suspensions and solution, J. Chem. Phys 20 (4) (1952) 571–581.
[53] Y. Xuan, W. Roetzel, Conceptions for heat transfer correlation of nanofuids, Int. J. Heat Mass Transf. 43 (2000) 3701–3707.
[54] R. Vajjha, D. Das, Specific heat measurement of three nanofluids and development of new correlations, J. Heat Transfer 131 (7) (2009) 1–7.
[55] L. Zhou, B. Wang, X. Peng, X. Du, Y. Yang, On the specific heat capacity of CuO nanofluid, Adv. Mech. Eng. (2010) 1–4.
[56] T. Bergman, Effect of reduced specific heats of nanofluids on single phase, laminar internal forced convection, Int. J. Heat Mass Transf. 52 (2009) 1240–1244.
[57] R. Mei, L.S. Luo, W. Shyy, An accurate curved boundary treatment in the lattice boltzmann method, J. Comput. Phys. 155 (1999) 307–330.
[58] O. Filippova, D. Hanel, Grid refinement for lattice-BGK models, J. Comput. Phys. 147 (1998) 219–228.
[59] O. Filippova, D. Hanel, Lattice-boltzmann simulation of gas-particle flow in filters, Comput. Fluids 26 (1997) 697–712.
[60] R. Mei, W. Shyy, D. Yu, L.S. Luo, Lattice Boltzmann method for 3-D flows with curved boundary, J. Comput. Phys. 161 (2000) 680–699.
[61] A. Kherbeet, H. Mohammed, B. Salman, H.E. Ahmed, O.A. Alawi, Experimental and numerical study of nanofluid flow and heat transfer, Int. J. Heat Mass Transf. 79 (2014) 858–867.